Gradient computation for full-waveform inversion of microseismic data in VTI media

Oscar Jarillo Michel and Ilya Tsvankin
Center for Wave Phenomena, Colorado School of Mines

ABSTRACT

Source locations are usually estimated from microseismic data using kinematic techniques. Full-waveform inversion (FWI) can potentially provide more accurate source parameters along with an improved velocity model by incorporating information contained in the entire trace including the coda. Here, we address one of the key issues in implementing FWI for microseismic surveys — efficient calculation of the gradient of the objective function with respect to the model parameters. Application of the adjoint-state method helps obtain closed-form expressions for the gradients with respect to the source location and moment tensor. Computation of the forward and adjoint wavefields is performed with a finite-difference algorithm that handles elastic VTI (transversely isotropic with a vertical symmetry axis) models. Numerical examples illustrate the properties of the gradients for the wavefield from a moment-tensor source in homogeneous and layered VTI media.

Key words: full-waveform inversion, adjoint-state method, anisotropy, transverse isotropy, dislocation source, moment tensor

1 INTRODUCTION

Microseismicity has developed in recent years as an efficient technique for reservoir monitoring (Maxwell, 2010; Kendall et al., 2011). Microseismic experiments typically involve recording the seismic response to hydraulic fracturing of tight reservoirs, most often shales. The location of the induced microfractures, as well as the origin time of the corresponding seismic events can be inferred from the data acquired in an observation borehole or at the surface. Usually only a single borehole is available, but it is highly beneficial to record microseismic data in several boreholes.

Accurate location of microseismic events requires knowledge of the background velocity model. This initial model is usually obtained from sonic logs and traveltimes of the direct P- and S-waves excited by perforation shots and recorded by geophones deployed in a monitor borehole. Afterwards, the model can be updated using the traveltimes of microseismic events. Velocity analysis without adequately accounting for seismic anisotropy may lead to significant errors in event location. In particular, shales are known to be transversely isotropic and may become orthorhombic or possess an even lower symmetry due to fracturing (Tsvankin and Grechka, 2011; Tsvankin, 2012). Van Dok et al. (2011) highlight the sensitivity of estimated event locations to the anisotropy parameters of TI media. Grechka et al. (2011) demonstrate that anisotropic velocity models constructed while locating microseismic events provide more accurate source locations than those obtained with models based solely on sonic logs and perforation shots.

It is also important to study the source mechanism associated with microseismic events because it can reveal important information about the rupture process. Earthquake point sources are described by the second-rank symmetric seismic moment tensor M_{ij} with six independent elements. As discussed by Vavryčuk (2007), all components of the moment tensor for microseismic events can be retrieved from the amplitudes of P-waves recorded in three boreholes or from P- , SV-, and SH-wave amplitudes measured in two boreholes. For events located in the $[x_1, x_3]$-plane of a 2D azimuthally isotropic model, the in-plane polarized waves depend on the moment tensor elements M_{11}, M_{13}, and M_{33}, which can be found from P- and SV-waves recorded in a single borehole. Depending on the receiver geometry and distribution of sources, microseismic data potentially can help estimate the pertinent anisotropy parameters (Grechka and Duchkov, 2011) and the source location (Grechka et al., 2011).

Most existing methods of event location are based on kinematic inversion that replaces a seismic trace with the band-limited δ-functions corresponding to the direct arrivals, which restricts the resolution according to the Rayleigh criterion (i.e., two sources appear as one if the distance between them is

smaller than one-half of the predominant wavelength). Considering the increasing usage of back-projection techniques and the rich information content of microseismic data, improved results can be expected from full-waveform inversion (FWI). Indeed, FWI operates with the entire trace including scattered waves, so the results are not subject to the Rayleigh criterion. Hence, for typical wavelengths in downhole microseismic surveys, one can expect substantially reduced event-location errors. Another potential benefit of FWI is an improved accuracy of the velocity model.

FWI is used to build high-resolution velocity models from seismic data using phase and, sometimes, amplitude information (Tarantola, 1984; Gauthier et al., 1986; Mora, 1987; Pratt, 1999; Virieux and Operto, 2009). Recently FWI has been extended to elastic and anisotropic media (Lee et al., 2010; Kamath and Tsvankin, 2013), which makes it suitable for multicomponent reflection and microseismic data.

The objective function in FWI quantifies the difference between observed and predicted data in the time or frequency domain. Efficient inversion requires application of iterative optimization schemes such as the conjugate-gradient method, which involves calculation of the gradient of the objective function with respect to the model parameters. In principle, the gradient can be found from the Fréchet derivatives obtained by differentiating the wavefield with respect to each model parameter. However, if the number of unknowns is large, computation of the Fréchet derivatives becomes prohibitively expensive.

A computationally efficient alternative for computing the gradient and model updating without the Fréchet derivatives is the adjoint-state method (Plessix, 2006; Fichtner et al., 2006; Fichtner, 2009; Köhn, 2011). This method makes it possible to calculate the gradient using just two forward-modeling simulations: first to generate the forward wavefield, which yields the predicted data, and second to compute the adjoint wavefield.

There has been significant progress in applying adjoint methods to tomographic velocity analysis and source-parameter inversion in global seismology. Tromp et al. (2005) and Liu and Tromp (2006) employ an adjoint formulation based on the Lagrangian-multiplier method to derive the gradients for the P- and S- wave velocities in isotropic media. They also analyze the sensitivity (Fréchet) kernels for 2D and 3D velocity models. Kim et al. (2011) obtain gradient expressions for the source parameters using the adjoint-state method and implement conjugate-gradient inversion to estimate the moment tensor, location, and source time function for an earthquake in Southern California using a known isotropic velocity model. Morency and Mellors (2012) follow the same approach to evaluate the moment tensor and source location of a geothermal event.

Here, we discuss the gradient computation for full-waveform inversion of microseismic data. The current algorithm is designed to estimate only the source location and moment tensor from 2D microseismic experiments.

We start by describing elastic finite-difference modeling for dislocation-type sources in VTI media. The adjoint-state method is then employed for efficient gradient calculation by adapting to our problem the general expressions for the gradients obtained by Kim et al. (2011). Although we plan to estimate the interval Thomsen parameters of layered VTI media as well, the current formulation is limited to the gradients for the source parameters. The performance of the algorithm is illustrated by synthetic examples for homogeneous and layered VTI media which include the wavefields obtained by forward and adjoint finite-difference modeling and the gradients calculated for the source location and moment tensor.

2 FORWARD MODELING

2.1 Implementation

The wave equation for a homogeneous anisotropic medium can be written as (Tsvankin, 2012):

$$\rho \frac{\partial^2 u_i}{\partial t^2} - c_{ijkl} \frac{\partial^2 u_k}{x_j x_l} = f_i \,, \tag{1}$$

where $\mathbf{u}(\mathbf{x},t)$ is the displacement field, c_{ijkl} is the stiffness tensor ($i,j,k,l = 1,2,3$), $\rho(\mathbf{x})$ is density, $\mathbf{f}(t)$ is the body force, and t is time.

Dislocation-type sources are described by the seismic moment tensor,

$$\mathbf{M} = \begin{pmatrix} M_{11} & M_{12} & M_{13} \\ M_{21} & M_{22} & M_{23} \\ M_{31} & M_{32} & M_{23} \end{pmatrix} , \tag{2}$$

which can be incorporated into the source term of equation 1 by using the notion of equivalent force (Aki and Richards, 1980; Dahlen and Tromp, 1998):

$$\rho \frac{\partial^2 u_i}{\partial t^2} - c_{ijkl} \frac{\partial^2 u_k}{\partial x_j \partial x_l} = M_{ij} \frac{\partial[\delta(\mathbf{x}-\mathbf{x}_s)]}{\partial x_j} S(t) \,, \tag{3}$$

where $\mathbf{x}_s$ is the source location, $S(t)$ is the source time function and $\delta(\mathbf{x}-\mathbf{x}_s)$ is the spatial δ-function. A common numerical approach for solving equation 3 exactly is finite differences (FD) (e.g., Graves, 1996). To describe 2D dislocation-type sources in a FD algorithm, Coutant et al. (1995) develop a formulation based on stress discontinuities.

2.2 Modeling examples

We carry out forward modeling for gradient computation in VTI media with moment-tensor sources using the elastic finite-difference code `sfewe` in MADAGASCAR . The model is described by the Thomsen parameters (Thomsen, 1986; Tsvankin, 2012) — the P- and S-wave vertical velocities V_{P0} and V_{S0} and the anisotropy coefficients ε, δ, and γ. In the case of P- and SV-waves propagating in the $[x_1,x_3]$-plane, the wavefield is not influenced by γ. An important combination of Thomsen parameters is the coefficient $\sigma \equiv (V_{P0}/V_{S0})^2(\varepsilon-\delta)$,

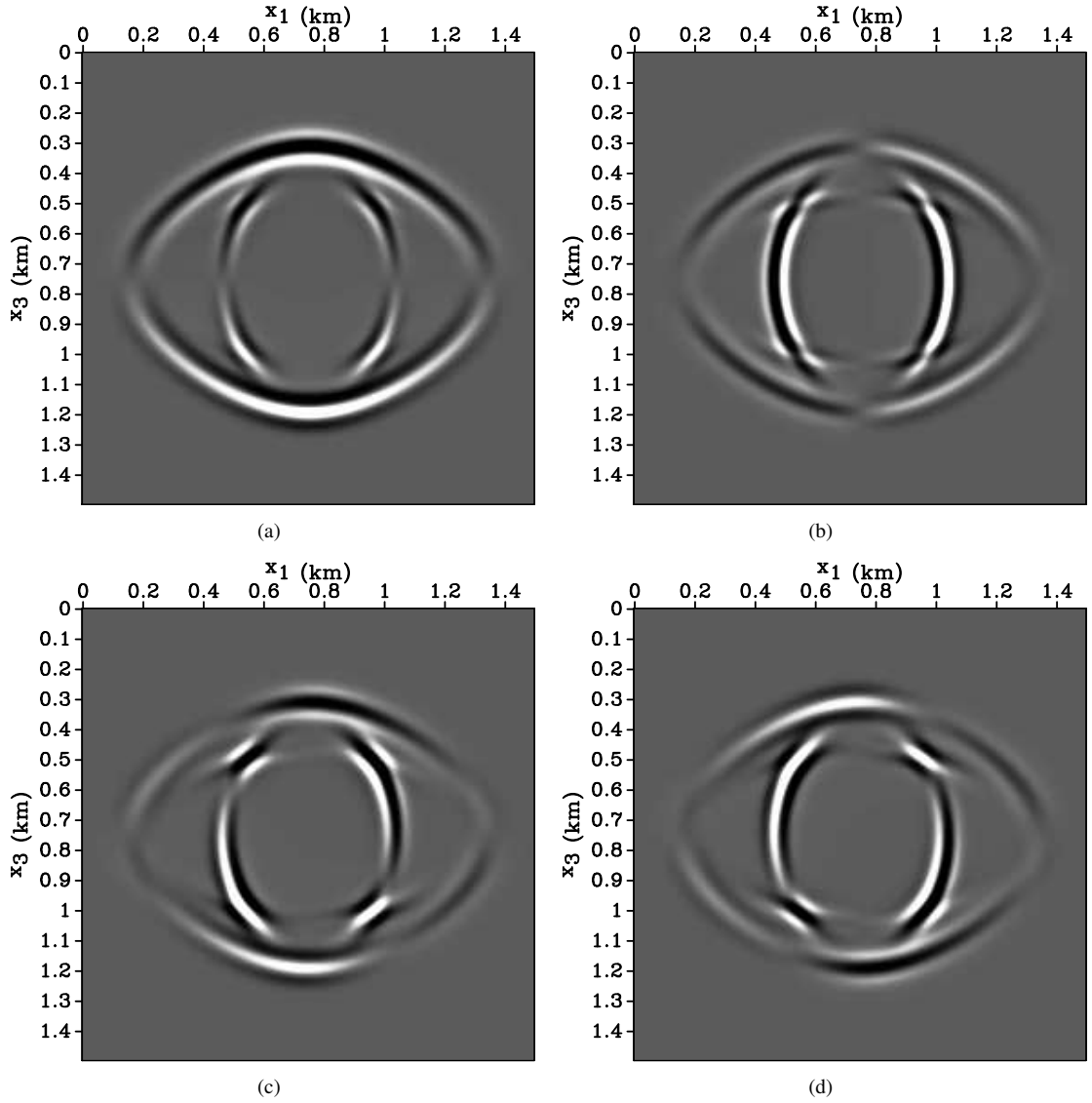

Figure 1. Vertical displacement generated by different moment-tensor sources in a homogeneous VTI medium. The medium parameters are $\rho = 2$ g/cm^3, $V_{P0} = 4047$ m/s, $V_{S0} = 2638$ m/s, $\varepsilon = 0.4$, and $\delta = 0$ ($\sigma = 0.94$). The source moment tensor is defined in the coordinate system rotated by the angle θ with respect to the horizontal (x_1) axis. The source parameters are: (a) $M_{11} = 4{\cdot}10^{10}$ Nm, $M_{13} = 0$, and $M_{33} = 4{\cdot}10^{10}$ Nm; (b) $M_{11} = 0$, $M_{13} = 4{\cdot}10^{10}$ Nm, $M_{33} = 0$, and $\theta = 0°$; (c) $M_{11} = 0$, $M_{13} = 4{\cdot}10^{10}$ Nm, $M_{33} = 0$, and $\theta = 45°$; and (d) $M_{11} = 0$, $M_{13} = 4{\cdot}10^{10}$ Nm, $M_{33} = 0$, and $\theta = 90°$.

which is largely responsible for the kinematic signatures of SV-waves in TI media.

The wavefields generated by explosive and dislocation-type sources in a homogeneous VTI medium are shown in Figure 1. The moment tensor is defined under the assumption that the medium around the source is locally isotropic. Due to the influence of anisotropy, a purely explosive source generates intensive S-waves in addition to P-waves (Figure 1 (a)). Figure 1 (b), (c), (d) display the wavefields excited by double-couple sources with different orientation (the corresponding rotation of the moment tensor is described in Appendix A). Rotation of the source causes pronounced changes in the radiation pattern of both P- and S-waves, which indicates the possibility of constraining the source orientation using FWI.

3 GRADIENTS FROM THE ADJOINT-STATE METHOD

3.1 Inverse problem

A mentioned above, the P- and SV-waves recorded in the $[x_1, x_3]$-plane depend on the components M_{11}, M_{13}, and M_{33} of the moment tensor. Originally, we invert just for these three

moment-tensor elements and the source coordinates x_1 and x_3 assuming that the velocity model and origin time are known.

The observed data $\mathbf{d}_{\text{obs}}$ and predicted data $\mathbf{d}_{\text{pre}}$ are produced by two forward simulations, where $\mathbf{d}_{\text{pre}}$ is obtained after modifying the source parameters used to generate $\mathbf{d}_{\text{obs}}$. In both cases, the elastic displacement field $\mathbf{u}(\mathbf{x}_{\text{s}}, \mathbf{x}_{\text{r}_n}, t)$ excited by a source located at $\mathbf{x}_{\text{s}}$ is recorded by N receivers located at $\mathbf{x}_{\text{r}_n}$ $(n = 1, 2, ..., N)$. Note that the source locations for the observed and predicted data may be different. The data residuals are measured by the least-squares objective function, which has to be minimized by the inversion algorithm:

$$\mathcal{F}(\mathbf{m}) = \frac{1}{2} \left\| \mathbf{d}_{\text{obs}} - \mathbf{d}_{\text{pre}}(\mathbf{m}) \right\|^2 . \tag{4}$$

3.2 Application of the adjoint-state method

The objective function depends on the model parameters through the state variables, which represent the solution of the forward-modeling equations. In our case, the state variable is the elastic displacement field $\mathbf{u}(\mathbf{x}, t)$ generated by a microseismic source and governed by equation 3.

The conjugate-gradient method involves calculation of the model update at each iteration. The update direction is determined by the derivatives of the objective function with respect to the model parameters, $\partial \mathcal{F}(\mathbf{m}) / \partial \mathbf{m}$. The adjoint-state method allows us to find this gradient for the entire set of model parameters in just two modeling simulations. However, because this method does not calculate the Fréchet derivatives, it is impossible to evaluate the sensitivity of the solution to measurement errors.

The adjoint-state method involves four main steps (Perrone and Sava, 2012):

(i) Computation of the state variable (forward wavefield).
(ii) Computation of the adjoint source.
(iii) Computation of the adjoint-state variable (adjoint wavefield).
(iv) Computation of the gradient of the objective function.

In addition to equation 3, the method requires solving the adjoint wave equation:

$$\rho \frac{\partial^2 u_i^\dagger}{\partial t^2} - c_{ijkl} \frac{\partial^2 u_k^\dagger}{\partial x_j \partial x_l} = \sum_{n=1}^{N} (\mathbf{d}_{\text{obs}} - \mathbf{d}_{\text{pre}})(T - t)\, \delta(\mathbf{x} - \mathbf{x}_{\text{r}_n}) , \tag{5}$$

where $\mathbf{u}^\dagger$ is called the adjoint wavefield. The so-called adjoint source on the right-hand side of equation 5 is obtained by differentiating the objective function $\mathcal{F}(\mathbf{m})$ with respect to the forward wavefield $\mathbf{u}$, and consists of the time-reversed data residuals. Therefore, the adjoint simulation can be carried out with the same modeling code by "injecting" the adjoint source at the receiver locations and then running the forward simulation.

The gradients of the objective function with respect to the moment-tensor elements and source coordinates can be found as (Kim et al., 2011):

$$\frac{\partial \mathcal{F}}{\partial M_{ij}} = \int_0^T \varepsilon_{ij}^\dagger(\mathbf{x}_{\text{s}}, t)\, S(T - t)\, \mathrm{d}t , \tag{6}$$

$$\frac{\partial \mathcal{F}}{\partial x_i} = \int_0^T \frac{\partial [\mathbf{M} : \boldsymbol{\varepsilon}^\dagger(\mathbf{x}_{\text{s}}, t)]}{\partial x_i}\, S(T - t)\, \mathrm{d}t , \tag{7}$$

where T is the recording time, $\boldsymbol{\varepsilon}^\dagger = \frac{1}{2}[\nabla \mathbf{u}^\dagger + (\nabla \mathbf{u}^\dagger)^{\text{T}}]$ is defined as the adjoint stress tensor, and $\mathbf{M} : \boldsymbol{\varepsilon}^\dagger$ is the double inner product of the tensors $\mathbf{M}$ and $\boldsymbol{\varepsilon}^\dagger$. Equations 6 and 7 applied to the 2D problem yield the gradient vector $\mathbf{g}$ for the five source parameters:

$$\mathbf{g} = \left\{ \frac{\partial \mathcal{F}}{\partial M_{11}}, \frac{\partial \mathcal{F}}{\partial M_{13}}, \frac{\partial \mathcal{F}}{\partial M_{33}}, \frac{\partial \mathcal{F}}{\partial x_1}, \frac{\partial \mathcal{F}}{\partial x_3} \right\} . \tag{8}$$

It is interesting that in contrast to the gradients for velocity-related parameters (Liu and Tromp, 2006), which depend on the interaction between the forward and adjoint wavefields, equations 6 and 7 include only the adjoint wavefield. Therefore, there is no need to store the forward wavefield or to recalculate it during the adjoint simulation performed for computing the gradients.

In application of FWI to velocity analysis, the adjoint wavefield is supposed to "illuminate" the erroneous parts of the velocity model. Likewise, for the source-inversion problem, the adjoint wavefield should reveal the portion of the model that causes the differences between the observed and predicted data. The discrepancy, however, is attributed to errors in the source parameters. In principle, the number of sources in the adjoint problem is unrestricted. If the forward wavefield is excited by multiple sources, the adjoint wavefield may focus at each source location, and application of equations 6 and 7 is supposed to enhance the focusing.

4 NUMERICAL RESULTS

Next, we present the results of synthetic tests for a homogeneous VTI medium and a stack of three constant-density VTI layers, with the wavefield modeled using the FD code mentioned above.

In the first experiment (Figure 2), the observed and initial predicted data (Figures 3 and 4) are generated for a single microseismic event recorded in a vertical "borehole" by receivers located at each grid point. The large number of receivers helps to reduce artifacts due to the sparse receiver coverage. Whereas the observed field is generated by a double-couple source, the predicted field is computed with an explosive source. Next, the adjoint source "injected" at the receiver locations is used to compute the adjoint wavefield (Figure 5). This wavefield focuses at the time $t = 0.462$ s near the actual source, where the model perturbation is located. The focusing time corresponds to the raypath between the source and the receivers located at the end of the array.

After applying equations 6 and 7, we obtain the gradients for the five source parameters shown in Figure 6. As ex-

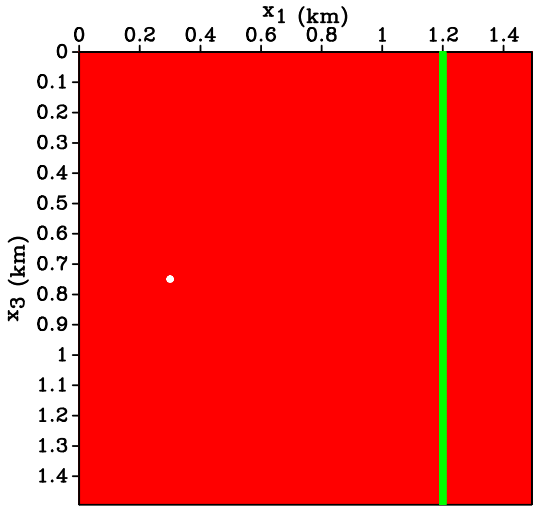

Figure 2. Source (white dot) and a vertical line of receivers at $x_1 = 1.2$ km embedded in a homogeneous VTI medium. The receivers are placed at each grid point (every 0.6 m). The medium parameters are $\rho = 2$ g/cm^3, $V_{P0} = 4047$ m/s, $V_{S0} = 2638$ m/s, $\varepsilon = 0.4$, and $\delta = 0$. The source is located at $x_1 = 0.3$ km, $x_3 = 0.75$ km.

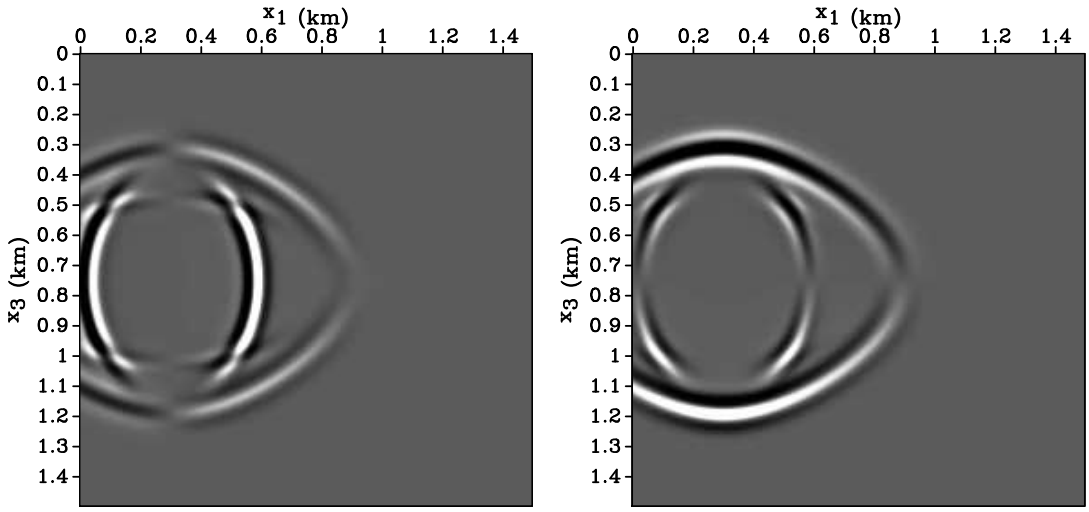

Figure 3. Snapshots of the vertical displacement for the model in Figure 2 at $t = 0.175$ s. (a) The observed wavefield produced by a double-couple source with $M_{11} = 0$, $M_{13} = 4{\cdot}10^{10}$ Nm, $M_{33} = 0$, and $\theta = 0°$. (b) The predicted wavefield from an explosive source with $M_{11} = 4{\cdot}10^{10}$ Nm, $M_{13} = 0$, and $M_{33} = 4{\cdot}10^{10}$ Nm.

pected, the major contribution to the gradients comes from the focusing of the adjoint wavefield near the source location. The additional anomalies are artifacts, likely due to the finite duration of the signal and limited number of sources and receivers (Fichtner et al., 2006). The significant magnitude of the gradients for x_1 and x_3 seems to be surprising because the locations of the observed and predicted sources coincide. However, the gradients for the source coordinates depend on the components of the moment tensor (equation 7), which produces the anomalies in Figure 6 (a), (b).

The second test is performed for the three-layer VTI model in Figure 7. The data are generated for a microseismic event occurring in the middle layer and recorded in a vertical "borehole". The gradients calculated using the forward and adjoint simulations are shown in Figure 8. As expected, layer boundaries create a number of reflected and mode-converted waves. However, the main contribution to the gradient still comes from the model perturbation at the source location.

For the third experiment, we keep the actual source at the same place as in the previous tests and use the homogeneous model from Figure 2. However, the initial predicted source is moved to a different location (Figure 9), which causes signifi-

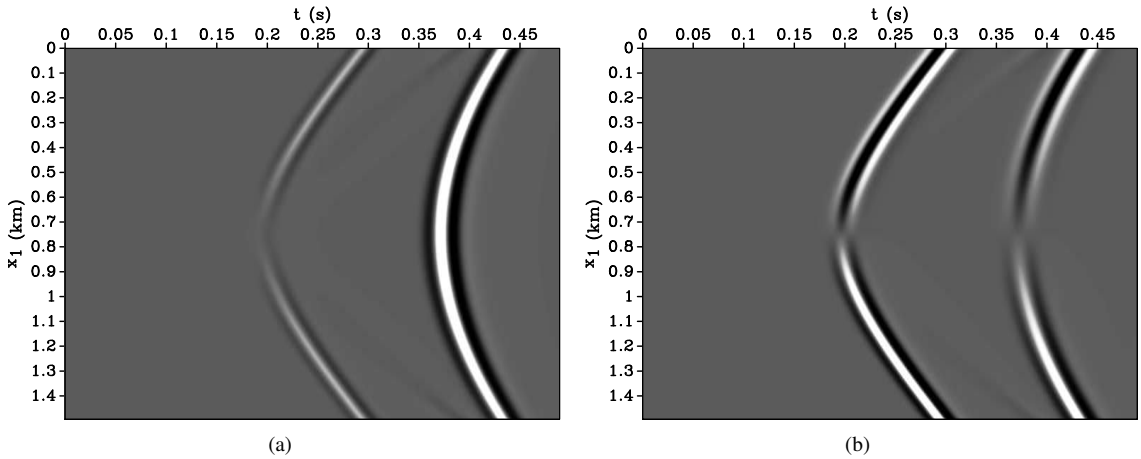

Figure 4. Vertical displacement of the (a) observed and (b) predicted data for the model in Figure 2 generated with the source parameters from Figure 3.

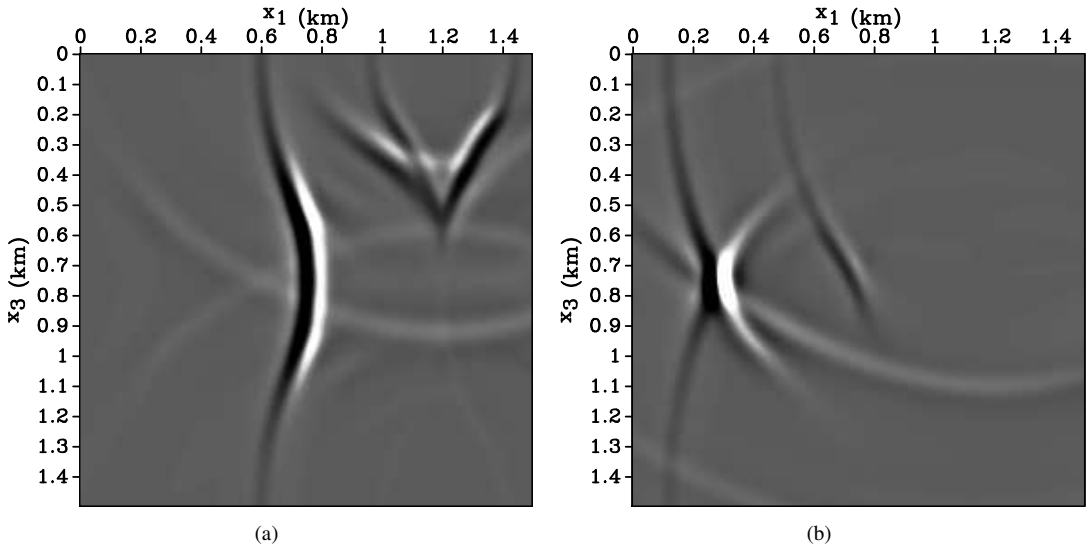

Figure 5. Snapshots of the vertical component of the adjoint wavefield for the model in Figure 2 at times (a) $t = 0.280$ s and (b) $t = 0.462$ s. The adjoint wavefield focuses at the actual source location on plot (b).

cant changes in the gradients (Figure 10). In particular, shifting the predicted source generates pronounced gradient contributions at both source locations. It is encouraging, however, that the largest gradients are observed near the predicted source. Although both sources have the same moment tensor, the gradients for M_{11}, M_{13}, and M_{13} do not vanish because the wavefield substantially changes with source location.

5 CONCLUSIONS

The adjoint-state method provides a computationally efficient way to calculate the gradients of the objective function. Here, we implemented adjoint-wavefield modeling and gradient computation of the FWI gradient for the source location and moment tensor using a known VTI velocity model.

Synthetic tests were carried out for a single source and a dense array of receivers in a vertical "borehole." The first experiment was performed for a trial source with a distorted moment tensor correctly positioned in a homogeneous VTI medium. The adjoint wavefield focuses near the source location, which identifies the perturbed area. Although the source position was not changed, the gradients for the source coordinates do not vanish because they depend on the moment-tensor elements. The gradients are contaminated by artifacts, which can be suppressed by adding receivers in another borehole or at the surface.

The second test was performed for a three-layer VTI

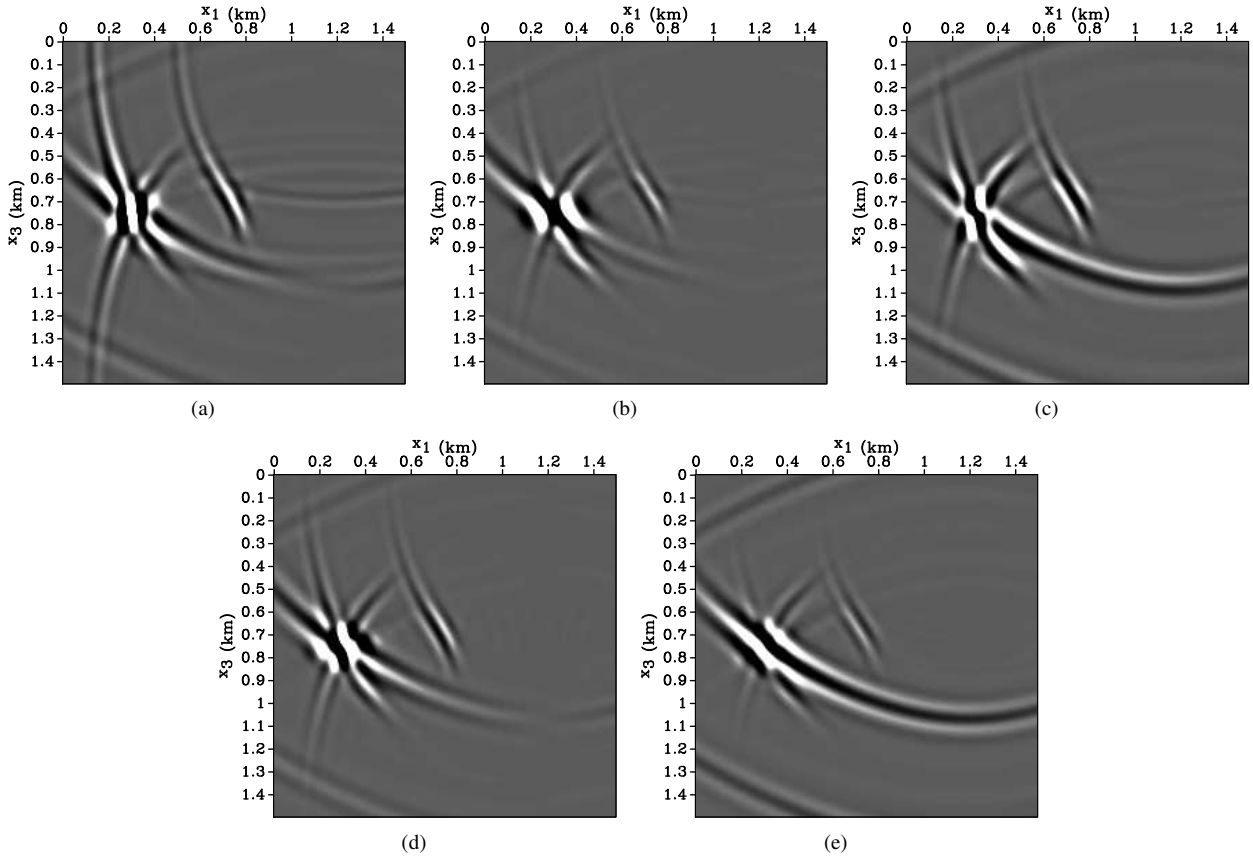

Figure 6. Gradients for the source parameters for the model in Figure 2: (a) M_{11}, (b) M_{13}, (c) M_{33}, (d) x_1, and (e) x_3.

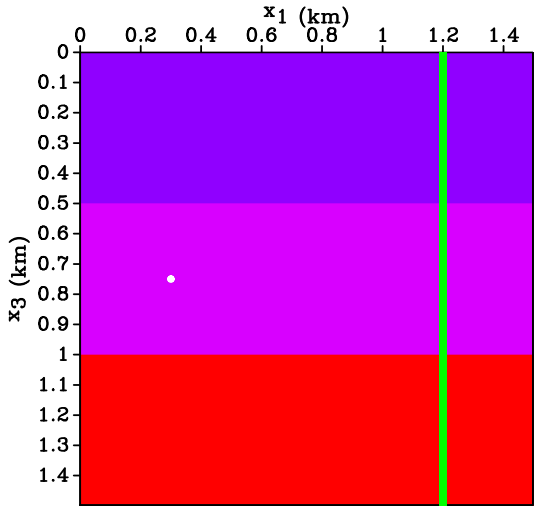

Figure 7. Three-layer VTI model used in the second experiment. The source-receiver geometry is the same as in Figure 2. The distance between receivers is 2.5 m. The parameters $\rho = 2$ kg/m^3, $\varepsilon = 0.4$, and $\delta = 0$ are the same in all three layers. The velocities in the first layer are $V_{P0} = 4047$ m/s and $V_{S0} = 2638$ m/s; for the second layer, $V_{P0} = 4169$ m/s and $V_{S0} = 2320$ m/s; for the third layer, $V_{P0} = 4693$ m/s and $V_{S0} = 2682$ m/s.

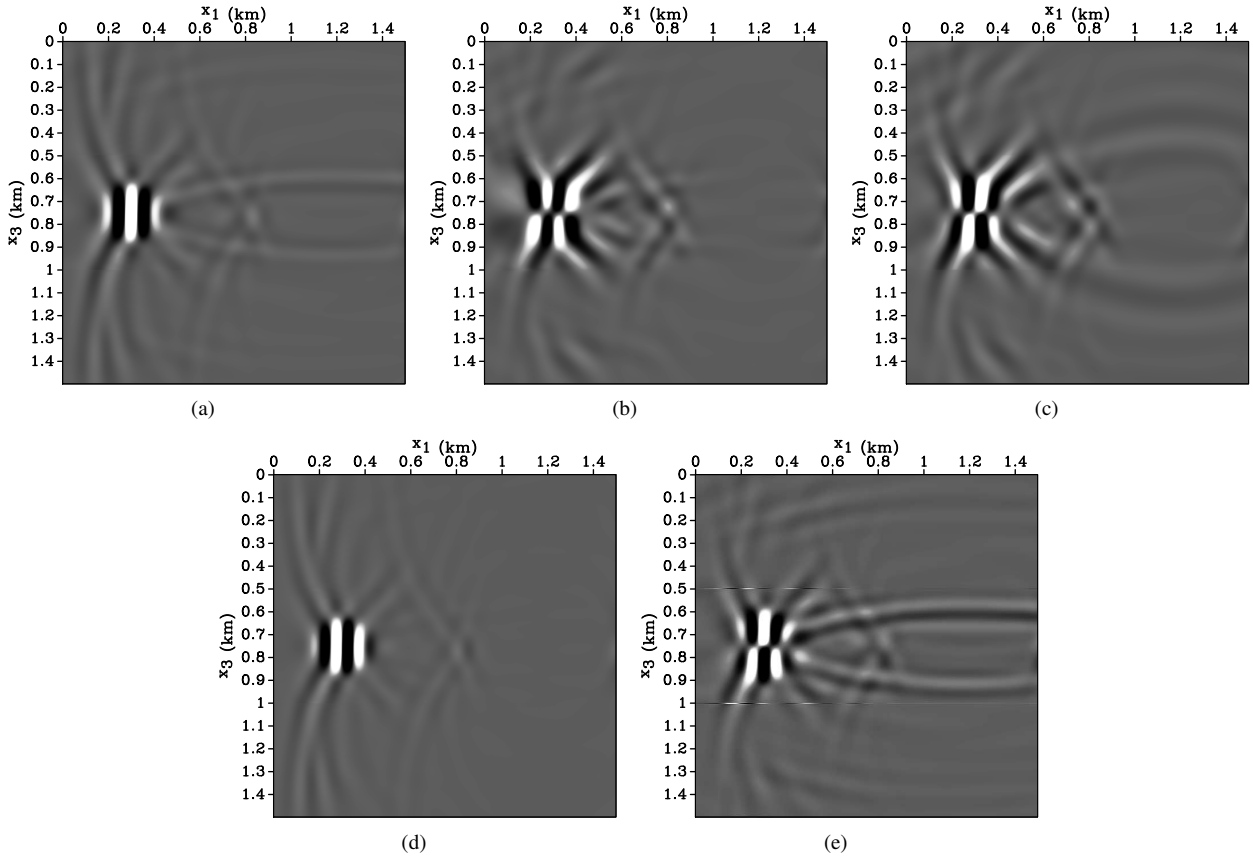

Figure 8. Gradients for the source parameters for the model in Figure 7: (a) M_{11}, (b) M_{13}, (c) M_{33}, (d) x_1, and (e) x_3.

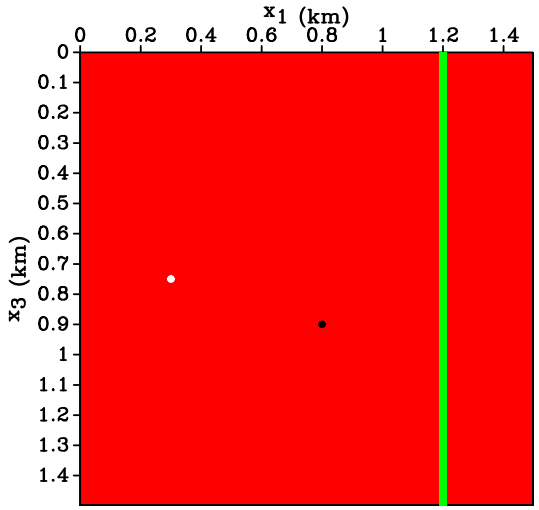

Figure 9. Actual source (white dot), predicted source (black dot) and a vertical line of receivers (spacing is 2.5 m) embedded in a homogeneous VTI medium. The medium parameters are the same as in Figure 2. The actual source is located at $x_1 = 0.3$ km, $x_3 = 0.75$ km and the predicted source is at $x_1 = 0.8$ km, $x_3 = 0.9$ km. The moment tensor for both sources corresponds to a horizontal ($\theta = 0$) double-couple with $M_{11} = 0$, $M_{13} = 4{\cdot}10^{10}$ Nm, and $M_{33} = 0$.

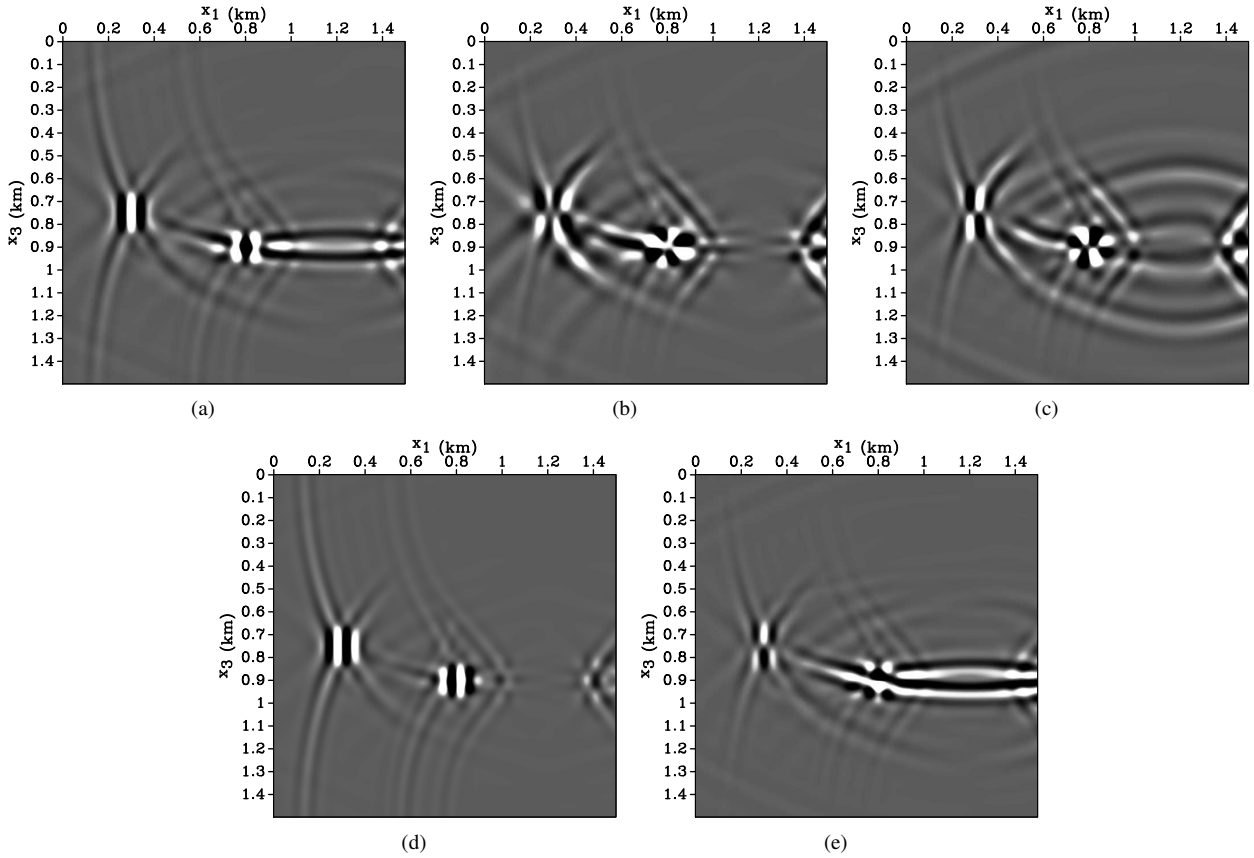

Figure 10. Gradients for the source parameters for the model in Figure 9: (a) M_{11}, (b) M_{13}, (c) M_{33}, (d) x_1, and (e) x_3.

model, which produces a number of reflected and converted waves. Although the gradients are more noisy, the anomaly at the source location is better focused due to the contribution of the additional events.

In the last test, the predicted wavefield was generated by a source with the correct moment tensor but erroneous location. The gradients for all source parameters, including the moment-tensor elements, exhibit pronounced anomalies, which are most intensive at the location of the trial source. These results indicate potential trade-offs between the source parameters in model updating using the conjugate-gradient method.

6 ACKNOWLEDGMENTS

We are grateful to Vladimir Grechka (Marathon Oil), who has generously provided valuable insights and feedback regarding various aspects of this work, and to Jeroen Tromp (Princeton University) for his advice on gradient calculation. We thank Esteban Díaz, Francesco Perrone, Nishant Kamath, and Steven Smith (all from CWP) for their technical assistance and help with the implementation of the adjoint problem. The numerical examples in this paper are produced with the MADAGASCAR open-source software package freely available at www.ahay.org. This work was supported by the Consortium Project on Seismic Inverse Methods for Complex Structures at the Center for Wave Phenomena (CWP).

APPENDIX A: 2D ROTATION OF THE MOMENT TENSOR

Dislocation-type events often occur along nonhorizontal fault planes. Here, we rotate the tensor **M** from the natural coordinate system associated with the fault to the $[x_1, x_3]$ coordinates.

The 2D rotation matrix **a** that produces a counterclockwise rotation is given by

$$\mathbf{a} = \begin{pmatrix} \cos\theta & -\sin\theta \\ \sin\theta & \cos\theta \end{pmatrix}. \tag{A1}$$

where θ is the angle between the x-axis in the natural coordinate system and the horizontal. The waves polarized in the $[x_1, x_3]$-plane are governed by the 2D moment tensor:

$$\mathbf{M} = \begin{pmatrix} M_{11} & M_{13} \\ M_{13} & M_{33} \end{pmatrix}. \tag{A2}$$

The moment tensor in the rotated coordinate system is then obtained as:

$$\mathbf{M}^{'} = \mathbf{a}\mathbf{M}\mathbf{a}^{\mathrm{T}}, \tag{A3}$$

where $\mathbf{a}^{\mathrm{T}}$ is the transpose of $\mathbf{a}$. The explicit expressions for each element of the rotated moment tensor are:

$$M_{11}^{'} = M_{11}\cos^2\theta - 2M_{13}\sin\theta\cos\theta + M_{33}\sin^2\theta, \tag{A4}$$

$$M_{13}^{'} = M_{11}\sin\theta\cos\theta + M_{13}(\cos^2\theta - \sin^2\theta) - M_{33}\sin\theta\cos\theta, \tag{A5}$$

$$M_{33}^{'} = M_{11}\sin^2\theta + 2M_{13}\sin\theta\cos\theta + M_{33}\cos^2\theta. \tag{A6}$$

Here, this rotation is used to obtain the predicted data for dislocation-type sources with different orientations.

REFERENCES

Aki, K., and P. G. Richards, 1980, Quantitative seismology theory and methods, volume I: W. H. Freeman and Company.

Coutant, O., J. Virieux, and A. Zollo, 1995, Numerical source implementation in a 2D finite difference scheme for wave propagation: Bulletin of the Seismological Society of America, **85**, 1507–1512.

Dahlen, F. A., and J. Tromp, 1998, Theoretical global seismology: Princeton University Press.

Fichtner, A., 2009, Full seismic waveform inversion for structural and source parameters: PhD thesis, Ludwig-Maximilians-Universität München.

Fichtner, A., H.-P. Bunge, and H. Igel, 2006, The adjoint method in seismology: I. Theory: Physics of the Earth and Planetary Interiors, **157**, 86–104.

Gauthier, O., J. Virieux, and A. Tarantola, 1986, Two-dimensional nonlinear inversion of seismic waveforms: Numerical results: Geophysics, **51**, 1387–1403.

Graves, R. W., 1996, Simulating seismic wave propagation in 3D elastic media using staggered-grid finite differences: Bulletin of the Seismological Society of America, **86**, 1091–1106.

Grechka, V., and A. Duchkov, 2011, Narrow-angle representations of the phase and group velocities and their applications in anisotropic velocity-model building for microseismic monitoring: Geophysics, **76**, WC127–WC142.

Grechka, V., P. Singh, and I. Das, 2011, Estimation of effective anisotropy simultaneously with locations of microseismic events: Geophysics, **76**, WC143–WC155.

Kamath, N., and I. Tsvankin, 2013, Full-waveform inversion of multicomponent data for horizontally layered VTI media: Geophysics.

Kendall, M., S. Maxwell, G. Foulger, L. Eisner, and Z. Lawrence, 2011, Microseismicity: Beyond dots in a box Introduction: Geophysics, **76**, WC1–WC3.

Kim, Y., Q. Liu, and J. Tromp, 2011, Adjoint centroid-moment tensor inversions: Geophysical Journal International, **186**, 264–278.

Köhn, D., 2011, Time domain 2D elastic full waveform tomography: PhD thesis, Christian-Albrechts-Universität zu Kiel.

Lee, H.-Y., J. M. Koo, D.-J. Min, B.-D. Kwon, and H. S. Yoo, 2010, Frequency-domain elastic full waveform inversion for VTI media: Geophysical Journal International, **183**, 884–904.

Liu, Q., and J. Tromp, 2006, Finite-frequency kernels based on adjoint methods: Bulletin of the Seismological Society of America, **96**, 2383–2397.

Maxwell, S., 2010, Microseismic: Growth born from success: The Leading Edge, **29**, 338–343.

Mora, P., 1987, Nonlinear two-dimensional elastic inversion of multioffset seismic data: Geophysics, **52**, 1211–1228.

Morency, C., and R. J. Mellors, 2012, Full moment tensor and source location inversion based on full waveform adjoint inversion: application at the Geysers geothermal field: SEG Technical Program Expanded Abstracts, 532, 1–5.

Perrone, F., and P. Sava, 2012, Wavefield tomography based on local image correlations: CWP Project Review Report, 51–76.

Plessix, R.-E., 2006, A review of the adjoint-state method for computing the gradient of a functional with geophysical applications: Geophysical Journal International, **167**, 495–503.

Pratt, R., 1999, Seismic waveform inversion in the frequency domain, Part 1: Theory and verification in a physical scale model: Geophysics, **64**, 888–901.

Tarantola, A., 1984, Inversion of seismic reflection data in the acoustic approximation: Geophysics, **49**, 1259–1266.

Thomsen, L., 1986, Weak elastic anisotropy: Geophysics, **51**, 1954–1966.

Tromp, J., C. Tape, and Q. Liu, 2005, Seismic tomography, adjoint methods, time reversal and banana-doughnut kernels: Geophysical Journal International, **160**, 195–216.

Tsvankin, I., 2012, Seismic signatures and analysis of reflection data in anisotropic media, third edition: Society of Exploration Geophysicists.

Tsvankin, I., and V. Grechka, 2011, Seismology of azimuthally anisotropic media and seismic fracture characterization: Society of Exploration Geophysicists.

Van Dok, R., B. Fuller, L. Engelbrecht, and M. Sterling, 2011, Seismic anisotropy in microseismic event location analysis: The Leading Edge, **30**, 766–770.

Vavryčuk, V., 2007, On the retrieval of moment tensors from borehole data: Geophysical Prospecting, **55**, 381 – 391.

Virieux, J., and S. Operto, 2009, An overview of full-waveform inversion in exploration geophysics: Geophysics, **74**, WCC1–WCC26.